Measurement prospects for Higgs decays to strange quark pairs with the future International Large Detector at the International Linear Collider

Matthew J. Basso[a], Valentina Maria Martina Cairo[b,c], Chris Damerell[d], Shin-ichi Kawada[e], Robert Orr[a], Jan Strube[f], Dong Su[b], Ariel Schwartzman[b], Tomohiko Tanabe[g], Junping Tian[h], Jerry Vav'ra[b], and Caterina Vernieri[b]

[a]Department of Physics, University of Toronto, 60 Saint George St., Toronto, Ontario, Canada
[b]SLAC National Accelerator Laboratory, 2575 Sand Hill Road, Menlo Park, California, USA
[c]Experimental Physics Department, CERN, Geneva, Switzerland
[d]Particle Physics Department, STFC Rutherford Appleton Laboratory, Harwell Science and Innovation Campus, Didcot, United Kingdom
[e]DESY, Notkestraße 85, 22607 Hamburg, Germany
[f]Department of Physics, University of Oregon, 1371 E 13th Avenue, Eugene, Oregon, USA
[g]Energy Accelerator Research Organisation (KEK), 1-1 Oho, Tsukuba, Ibaraki, 305-0801, Japan
[h]International Center for Elementary Particle Physics (ICEPP), University of Tokyo, Hongo 7-3-1, Bunkyo-ku, Tokyo, 113-0033, Japan

January 12, 2022

Contact Information:
Matthew J. Basso (matthew.joseph.basso@cern.ch)
Valentina Maria Martina Cairo (valentina.maria.cairo@cern.ch)

Abstract

This paper describes a novel algorithm for tagging jets originating from the hadronisation of strange quarks (strange-tagging) with the future International Large Detector (ILD) at the International Linear Collider (ILC). It also presents the first application of such a strange-tagger to a

Higgs to strange ($h \to s\bar{s}$) analysis with the initial hypothetical $2\,\mathrm{ab}^{-1}$ of data which will be collected by ILD during its first 10 years of data taking at $\sqrt{s} = 250\,\mathrm{GeV}$. Limits on the Standard Model Higgs-strange coupling strength modifier, κ_s, are derived at the 95% CL to be XXX. The paper includes as well a preliminary attempt to design an ideal detector capable of maximising strange-tagging performance.

1 Introduction

The experimental program at the Large Hadron Collider (LHC) [1] has clearly established Yukawa couplings of the 125 GeV Higgs (h) to the third generation of fermions. The ATLAS and CMS experiments [2, 3] have recently reported evidence that the Higgs boson decays into two muons [4, 5], which indicates for the first time that the Higgs boson interacts with second-generation leptons. At the same time, this is just a hint and not yet a complete exploration of the second generation Yukawa couplings, because these rare Higgs decay modes (i.e., to charm or strange quarks) are very challenging or nearly impossible to detect with the current detector capabilities. Furthermore, the large multi-jet background at the LHC inhibits the study of light quark couplings with inclusive $h \to q\bar{q}$ decays, in addition to the dominant $h \to b\bar{b}$ decay mode.

At the LHC, new algorithms for the identification of jets originating from the hadronisation of c-quarks (c-tagging) are gradually becoming available and enabling new searches for the decay of the Higgs boson to charm quarks. Less literature, however, is available about searches of Higgs boson decays to light quarks [6, 7, 8, 9, 10, 11].

Searches for exclusive Higgs boson decays to a ϕ or $\rho(770)$ meson and a photon have been suggested and experimentally tested [11] as a probe of the Higgs boson couplings to the strange-quark, or the up- and down-quarks, respectively. For these Higgs couplings there are no projections available and it will most likely remain out of direct experimental reach unless they are enhanced compared to Standard Model (SM) expectations. In fact, when considering Beyond the Standard Model (BSM) scenarios that allow for extended Higgs sectors, the possibilities open up dramatically. A class of BSM models [12], where the origin of the first and second generation fermion masses is an additional source of electroweak symmetry breaking, predicts large deviations from the SM values. A simple example is the two Higgs doublet model (2HDM) where one doublet (approximately identified as the 125 GeV Higgs) couples mainly to the third generation, while the second doublet couples mainly to the first and second generation. This results in very different decay branching ratios of the additional heavy Higgs bosons (H). The largest production mode of the neutral Higgs bosons would be from a $c\bar{c}$ initial state, while the charged Higgs bosons would be predominantly produced from a $c\bar{s}$ initial state. The most interesting decay modes include $H/A \to c\bar{c}$, $t\bar{c}$, $\mu\mu$, and $\tau\mu$ and $H^{\pm} \to c\bar{b}$, $c\bar{s}$, and $\mu\nu$.

Tagging strange jets comes with some difficulty, however. As shown in Table 1, bottom and charm jets can be differentiated based on the presence of 2 or 1 secondary vertices. Strange jets, which, excluding V^0's, have 0 secondary vertices, are only differentiated from light (i.e., up or bottom) jets based on the ability to reliably tag the presence of a strange hadron within the jet. Strange hadrons are also most often the leading particle in strange jets, as evident from

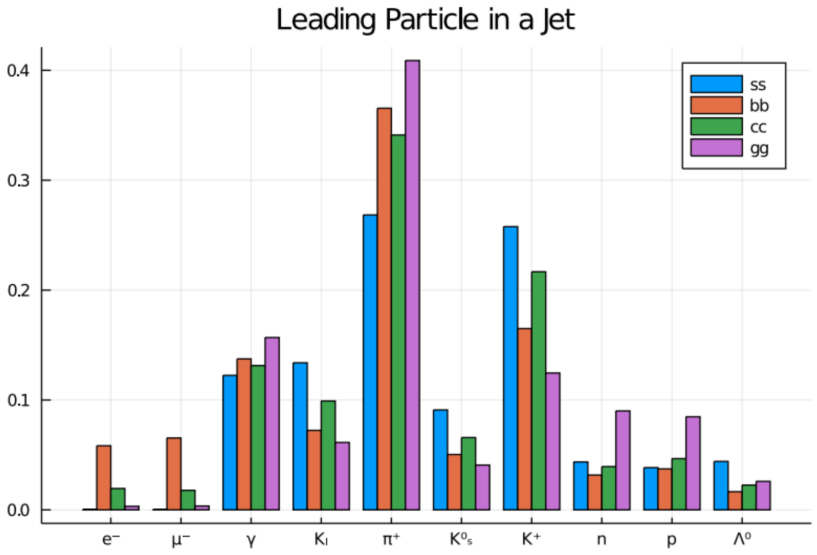

Figure 1: Leading particle fractions for reconstructed jets from $h \to s\bar{s}/b\bar{b}/c\bar{c}/gg$ events, generated using WHIZARD [13] and reconstructed with MARLIN [14] using a Silicon Detector [15] simulation. All of the bars of a particular colour sum to 1 by definition. Neutrinos and very soft ($E < 0.05\,\text{GeV}$) particles are excluded.

Figure 1. Accordingly, technology enabling kaon-pion discrimination is highly relevant at future detectors for measurements of decays to strange jets.

Table 1: Defining features for the different categories of quark jets.

Jet flavour	Number of secondary vertices (excluding V^0's)	Number of strange hadrons (e.g., $K^\pm$, $K^0_{L/S}$, and Λ^0)
Bottom	2	$\geq$1
Charm	1	$\geq$1
Strange	0	$\geq$1
Light	0	0

The work presented in this paper describes the novel development of a flavour tagging algorithm capable of tagging jets that originate from the hadronisation of strange quarks (strange-tagging). This allows us to tag for the first time exclusive Higgs decays and opens new opportunities in direct $h \to s\bar{s}$ searches. If used in conjunction with c-tagging, it also allows to probe new physics models. **[TODO: move the previous sentence to "Conclusions and next steps" if we do NOT include any $H \to cs$ studies here in the end]** The tagger is then applied to a SM (125 GeV) $h \to s\bar{s}$ analysis estimating the prospects for Higgs-strange coupling strength measurements.

Strange tagging itself is of interest in the context of the ILC study questions [16] proposed for Snowmass 2021 [17]. The study presented here is conducted in the context of the future International Linear Collider (ILC) [18], a

future electron-positron collider proposed to be built in Japan. Nevertheless, the results are easily applicable to future experiments at other electron-positron machines.

[**TODO: expand description of strange hadronisation.**]

The paper is organized as follows:

- Section 2 describes the International Large Detector, a proposed detector at the ILC and the detector used for the contained studies;
- Section 3 describes the Monte Carlo samples included in the study;
- Section 4 describes the development and validation of a jet flavour tagger using a neural network;
- Section 5 describes the application of the jet flavour tagger to a SM $h \to s\bar{s}$ analysis with ILD at the $\sqrt{s} = 250\,\text{GeV}$ ILC run;
- Section 6 describes a detector proposal which would maximize particle identification (PID) at high momenta and thus boost strange tagging performance.
- Section 7 describes the conclusions and next steps.

2 The ILD detector

The International Large Detector (ILD) is one of two detector concepts proposed at the ILC [19, 20, 21], the other being the Silicon Detector (SiD) [20, 15].

Closest to the interaction point, ILD has 3 double-layer pixel detectors for vertexing followed by a time projection chamber (TPC) for tracking. The TPC additionally provides PID via measurements of energy loss from charged particles due to ionisation (dE/dx) and time-of-flight (TOF) from inner and outer layers of silicon flanking the TPC. The low material budget of the TPC is highly desirable for low momentum tracking of particles.

Immediately beyond the tracking system, ILD has high granularity sampling calorimeters for particle flow reconstruction [22]. The precise design of the electromagnetic and hadronic calorimeters is still under study.

The tracking and calorimetry systems are contained within in a solenoid providing a 3.5 T magnetic field. A surrounding iron yoke instruments muon detection.

3 Monte Carlo simulation

The main Higgs boson production mechanism at the ILC is production in association with a Z boson ("associated production"), Zh. Accordingly, associated production is considered in this paper for generating the signal and some of the background events in both the $Z \to \nu\bar{\nu}$ and $Z \to \ell\ell$ decay channels. To a much smaller degree, ZZ- and WW-fusion production contribute in the $Z \to e^+e^-$ and $Z \to \nu_e\bar{\nu}_e$ decay channels, respectively; however, only ZZ-fusion is included in this paper.

The Monte Carlo (MC) events used in this study were generated at centre-of-mass energy $\sqrt{s} = 250\,\text{GeV}$ using WHIZARD 2.8.5 [13, 23] interfaced with

PYTHIA 6.4 [24] for showering/hadronisation, TAUOLA for polarised τ lepton decays [25, 26, 27], and GUINEA-PIG [28] and CIRCE2 [29, 30] for beam spectrum effects.

The generated events were reconstructed with MARLIN [14], using a full simulation of the ILD detector based on GEANT4 [31] in the MOKKA framework [32]. The reconstructed events were saved as DSTs, an LCIO[1] [34] event data model, and further refined as miniDSTs [35], a slimmed version of DST which also includes the results of the LCFIPlus [36] b-, c-, and $o-$ (i.e., "other" – strange, light, or gluon) jet tagger scores.

Low-p_{T} pileup from $\gamma\gamma \to$ hadrons events was simulated using the cross section model of Chen-Barklow-Peskin [37], reconstructed using the full ILD simulation, and overlaid onto all hard scatter events.

All MC samples are generated using 100% left-handed- (LH-) polarised electron beams and 100% right-handed- (RH-) polarised positron beams. As we consider the ILC running scenario at $\sqrt{s} = 250\,\mathrm{GeV}$ using 80% LH-polarised electron beams (i.e., $P_L[e^-] = -80\%$) and 30% RH-polarised positron beams (i.e., $P_R[e^+] = +30\%$), the polarisation-inclusive cross section σ_{inc} must be corrected. In particular, the 100% LH electron and 100% RH positron cross section σ_{LR} is given by:

$$\begin{aligned} \sigma_{LR} &= P_L P_R \sigma_{\mathrm{inc}} \\ &= \frac{1 - P_L[e^-]}{2} \frac{1 + P_R[e^+]}{2} \sigma_{\mathrm{inc}} \\ &= 0.585 \sigma_{\mathrm{inc}} \,. \end{aligned} \tag{1}$$

For this particular running scenario, an integrated luminosity $\mathcal{L}$ of $2\,\mathrm{ab}^{-1}$ is expected, as per the ILC physics programme [38]. Using the corrected cross sections and the expected luminosity, each sample is normalised prior to applying any analysis cuts, where the event weights are modified as:

$$w_i' = \frac{\mathcal{L}\sigma_{LR}}{\sum_j w_j} w_i \,\forall\, i \,, \tag{2}$$

where w_i is the weight for event i. N.B. there is no estimate available for the SM $h \to s\bar{s}$ branching ratio (BR), $\mathrm{BR}[h \to s\bar{s}]_{\mathrm{SM}}$ – instead, it is estimated by scaling the SM $h \to c\bar{c}$ BR, $\mathrm{BR}[h \to c\bar{c}]_{\mathrm{SM}}$, by the square of the ratio of the strange quark mass over the charm quark mass, M_s/M_c:

$$\begin{aligned} \mathrm{BR}[h \to s\bar{s}]_{\mathrm{SM}} &\approx \left(\frac{M_s}{M_c}\right)^2 \times \mathrm{BR}[h \to c\bar{c}]_{\mathrm{SM}} \\ &= 11.72^{-2} \times 0.0291 \\ &= 2 \times 10^{-4} \,. \end{aligned} \tag{3}$$

The ratio, $M_s/M_c = 11.72^{-1}$, is taken from the Particle Data Group (PDG) [39]. A similar procedure yields $\mathrm{BR}[h \to d\bar{d}]_{\mathrm{SM}} \approx 5 \times 10^{-7}$ and $\mathrm{BR}[h \to u\bar{u}]_{\mathrm{SM}} \approx 1 \times 10^{-7}$ using $M_s/M_d \sim 20$ and $M_u/M_d \approx 0.47$, also taken from the PDG [39].

[1] LCIO version 02-15-04 [33] was used for processing all of the input miniDSTs analysed in this paper.

The signal and background MC samples used in this study are shown in Table 2. Also shown are the raw numbers of events as well as the LR cross sections, per sample. The $h \to s\bar{s}$ comes

As a back-of-the-envelope calculation, assuming $2000\,\text{fb}^{-1}$ of data collected at the ILC after 10 years of data-taking and a Higgs boson production cross-section of about 200 fb, ∼400,000 Higgs bosons would be produced with only 80 of which feature a $h \to s\bar{s}$ event.

Table 2: MC processes considered in the $h \to s\bar{s}$ analysis, including raw statistics and cross sections. N.B. the samples were generated at $\sqrt{s} = 250\,\text{GeV}$ and the cross sections assume electron-positron beam polarisations of $P_L[e^-] = -80\%$ and $P_R[e^+] = +30\%$, respectively. The cross sections include the corresponding BRs for the indicated decays. In the non-Higgs processes, "nf" denotes the number (n) of fermions (f) in the final state. In $Z(\to \ell\ell)h(\to \text{other})$, "other" denotes any non-hadronic decay.

Process name	Raw events [a.u.]	LR cross section [fb]
$Z(\to \nu\bar{\nu})h(\to s\bar{s})$	500,000	0.021
$Z(\to \nu\bar{\nu})h(\to b\bar{b})$	500,000	58.1
$Z(\to \nu\bar{\nu})h(\to c\bar{c})$	499,800	2.9
$Z(\to \nu\bar{\nu})h(\to u\bar{u})$	499,800	1×10^{-5}
$Z(\to \nu\bar{\nu})h(\to d\bar{d})$	500,000	5×10^{-5}
$Z(\to \nu\bar{\nu})h(\to gg)$	499,800	8.6
$Z(\to \ell\ell)h(\to s\bar{s})$	373	0.011
$Z(\to \ell\ell)h(\to b\bar{b})$	872,380	29.8
$Z(\to \ell\ell)h(\to c\bar{c})$	43,334	1.5
$Z(\to \ell\ell)h(\to u\bar{u})$	0	6×10^{-6}
$Z(\to \ell\ell)h(\to d\bar{d})$	0	3×10^{-5}
$Z(\to \ell\ell)h(\to gg)$	123,225	4.4
$Z(\to \ell\ell)h(\to \text{other})$	460,688	15.9
$2f$ Z hadronic	25,354,400	127,965
$4f$ ZZ hadronic	7,099,000	1,405
$4f$ WW hadronic	14,790,600	14,866
$4f$ ZZ/WW hadronic	18,494,200	12,389
$2f$ Z leptonic	24,500,000	21,214
$4f$ ZZ semileptonic	4,199,600	838
$4f$ single Z semileptonic	6,999,600	1,423

4 Jet flavour tagger

In order to better tag strange, light, and gluon jets, an artificial neural network (ANN) was developed in Keras [40] using the TensorFlow backend [41]. The goal of tagging each jet by their flavour of progenitor particle (i.e., b, c, s, u/d, or g) inspires the use of a multiclassifier. The multiclassifier assigns a probability of a jet belonging to each possible output class (i.e., outputs a vector of size 5), and these probabilities logically sum up to 1 per jet.

4.1 Inputs

The training is performed on the $Z(\rightarrow \nu\bar{\nu})h(\rightarrow q\bar{q}/gg)$ samples from Table 2. All events are required to have $N_{\text{jets}} \geq 2$ and $N_{\text{leptons}} = 0$. The training is performed using only one jet per event, where the leading or subleading momentum jet is randomly chosen. Per process, 250,000 raw MC events are used – additionally, the $h \rightarrow u\bar{u}$ and $h \rightarrow d\bar{d}$ processes are combined into a single class, $h \rightarrow$ light.

As input to the ANN, several jet-level variables are chosen:

- kinematics: momentum p, pseudorapidity η, polar angle ϕ, and mass m;
- LCFIPlus tagger results: b-, c- and o-tag scores as well as jet category;
- number of Particle Flow Objects (PFOs – these are the particles which are grouped into the jet).

In addition to jet-level variables, it is prudent to include variables at the level of the PFOs contained within the jet. The 10 leading momentum particles contained within the jet have their kinematics redefined relative to the jet's axis and their momentum and mass scaled by the momentum of the jet. Per-particle, the following variables are also chosen as inputs:

- kinematics: p, η, ϕ, and m;
- charge q;
- truth likelihoods: $L(e^{\pm})$, $L(\mu^{\pm})$, $L(\pi^{\pm})$, $L(K)$, $L(p^{+})$.

The ILD detector will provide PID information per PFO, including electron ($e^{\pm}$), muon ($\mu^{\pm}$), pion ($\pi^{\pm}$), kaon (K), and proton (p^{+}) likelihoods, L. However, the reconstructed likelihoods utilising the dE/dx and TOF information were not available in the inputs at the time of the study. *Truth* likelihoods are assigned instead, representing a best-case scenario in terms of PID. The 5 truth likelihoods are assigned a binary number by comparing the absolute value of PDG ID [39] of the PFO to the PDG ID(s) of each particle class:

- electrons: 11;
- muons: 13;
- pions: 211;
- kaons: 310, 321, and 3122 (includes V^0's: K^0_s and Λ^0);
- protons: 2212;

where 1 is assigned if one of the PDGs match and 0 is assigned otherwise.

4.2 Architecture

PFO-level inputs motivates the use of a recurrent neural network (RNN), which can handle input events where the jet has fewer than 10 constituent particles (in these rare cases, the input vectors of particles are padded to size 10 with zero-initialised variables). A similar architecture (using a different flavour of

RNN) has been used for studying the maximum strange tagging performance at hadron machines [42]. The RNN consist of 3 layers using gated recurrent units (GRUs) [43]. The output from the RNN is concatenated with the jet-level inputs and serve as inputs to a multilayer perceptron (MLP) with 3 layers. Each layer of the MLP uses a scaled exponential linear unit (SELU) [44] activation, which has the nice property of self-normalising inputs. As the network is a multiclassifier, the sensible choice of output activation is the softmax function:

$$[f(\vec{x})]_i = \frac{\exp([\vec{x}]_i)}{\sum_{i=1}^{5} \exp([\vec{x}]_i)} \, \forall \, i = 1, \ldots, 5 \,, \tag{4}$$

where f is the softmax activation function, $\vec{x}$ is the input vector, and $[\ldots]_i$ denotes the i-th value of a vector. The output vector is of size 5, as there are 5 jet flavour classes, and sums to 1, by definition.

A pictorial representation of the network's architecture, including the number of nodes per layer, is shown in Figure 2.

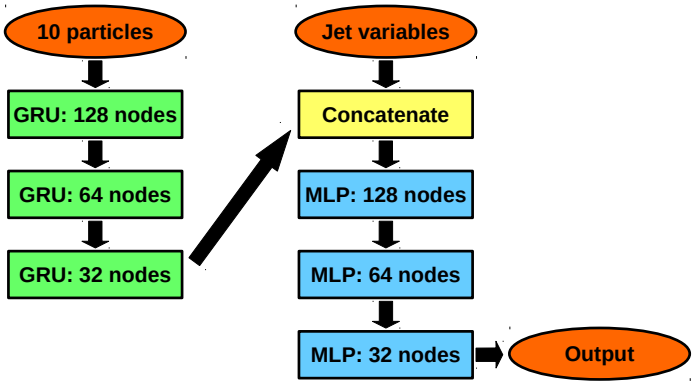

Figure 2: A cartoon of the network architecture used for the jet flavour tagger ANN. The arrows denote the flow of vectors through the network.

4.3 Training and validation

To train the network, input events are first split, where 90% of all events per class are reserved for training and 10% are reserved for testing. Within the training dataset, events are split according to even and odd event numbers. A two-way k-folding procedure is used, where the network is trained using only odd events and simultaneously validated using only even events ("k-fold 0"), and then the network is trained using only even events and simultaneously validated using only odd events ("k-fold 1"). In this way, the entire training dataset may be used. If the input vector for a given event is $\vec{x}$ and that same event has an event number n, then the output of the tagger, F is:

$$F(\vec{x}) = \begin{cases} F_{k\text{-fold}\,0}(\vec{x}) \,, & n \bmod 2 = 0 \\ F_{k\text{-fold}\,1}(\vec{x}) \,, & n \bmod 2 = 1 \end{cases} \,, \tag{5}$$

where $F_{k\text{-fold }0}$ is the output of network trained on k-fold 0 and $F_{k\text{-fold }1}$ is the output of network trained on k-fold 1. In this way, we avoid bias by ensuring the tagger is *never* applied to the same events it was trained on.

A categorical cross-entropy loss function is chosen, and the network is trained using the Adam [45] optimizer with a learning rate of 0.0005 and a batch size of 1024. Each class is re-normalised to have the same sum-of-weights. Early stopping is applied to prevent overtraining.

The output scores for each node of the k-fold 0 and 1 networks are shown in Figures 3 and 4, respectively. Each network is applied to both the "training" events (90% – includes both the actual events used in training as well as those used in validation) and to the testing events (10%). In all distributions, the training and testing are in good agreement with one another, indicating no overfitting occurred.

For both k-fold's 0 and 1, there is clear discrimination of b- and c-jets. Additionally, there is a capacity for *independently* tagging light-, s- and g-jets, but the separation power is somewhat reduced in comparison to b- and c-jets as these classes are more often confused with one another. This demonstrated by the confusion matrix shown in Figure 5, where there off-diagonal terms of order 10–20% in the upper 3×3 (i.e., gluon, light, and strange) matrix compared to off-diagonal terms of order 5–10% in the lower 2×2 (i.e., charm and bottom) matrix.

In order to quantify the performance of each network, the receiver-operator characteristic (ROC) curves (i.e., background rejection as a function of signal efficiency) are also calculated using Eq. 5 and shown in Figure 6. Alongside the tagger's ROC curves, the corresponding LCFIPlus results are also shown. Small improvements are seen for the b- and c-jet output nodes – likely, the tagger is simply returning the input LCFIPlus tagger scores with small enhancements due to the truth PID on the jet's constituent PFOs. However, large improvements are observed for light-, s-, and g-jet tagging when using the multiclassifier over the LCFIPlus OTagger.

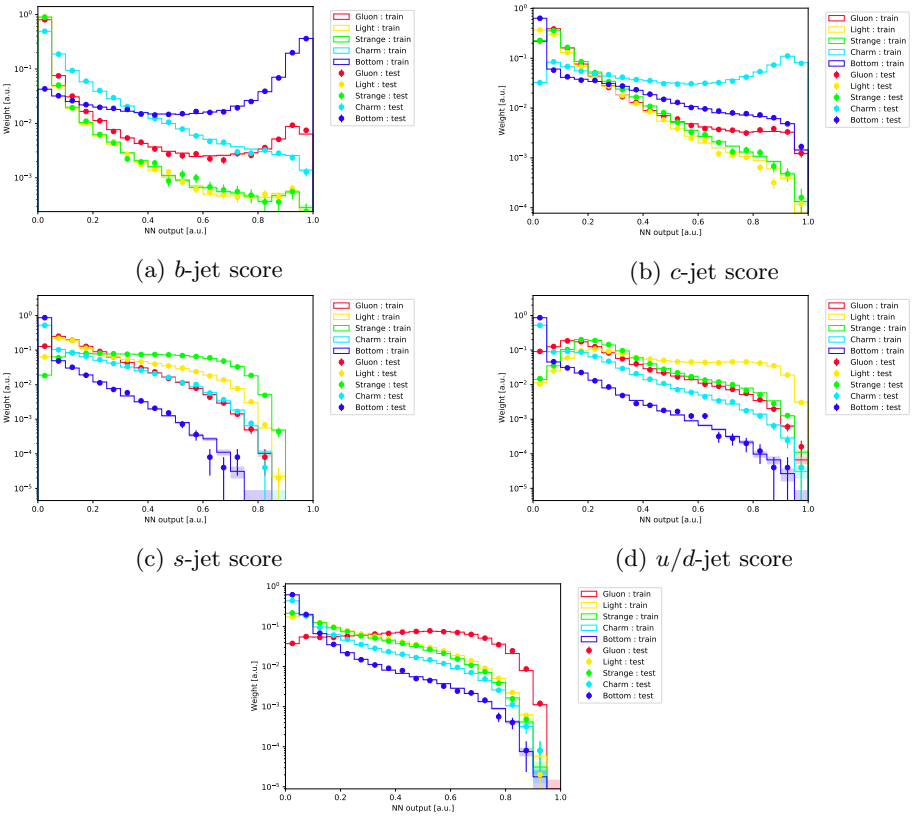

(a) b-jet score

(b) c-jet score

(c) s-jet score

(d) u/d-jet score

(e) g-jet score

Figure 3: Distributions of the ANN's output nodes for the training and testing slices of k-fold 0. N.B. each class of each slice is normalised to the same sum-of-weights (i.e., 1) and logarithmic y-axis scales are used. The error bars correspond to Poisson counting statistics.

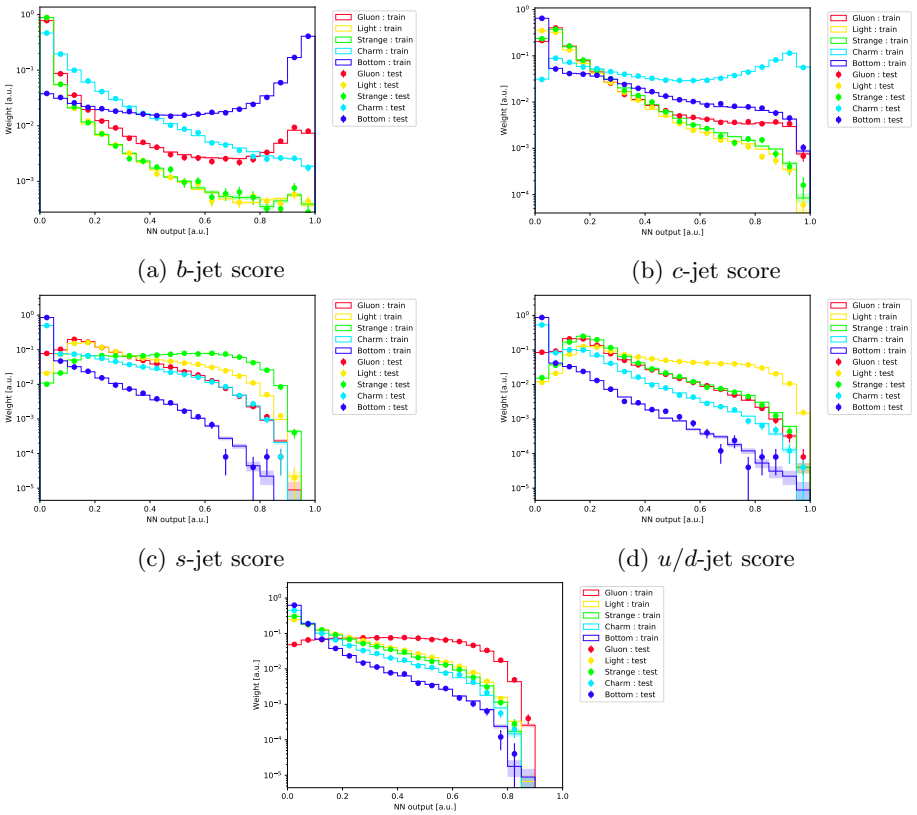

(a) b-jet score

(b) c-jet score

(c) s-jet score

(d) u/d-jet score

(e) g-jet score

Figure 4: Distributions of the ANN's output nodes for the training and testing slices of k-fold 1. N.B. each class of each slice is normalised to the same sum-of-weights (i.e., 1) and logarithmic y-axis scales are used. The error bars correspond to Poisson counting statistics.

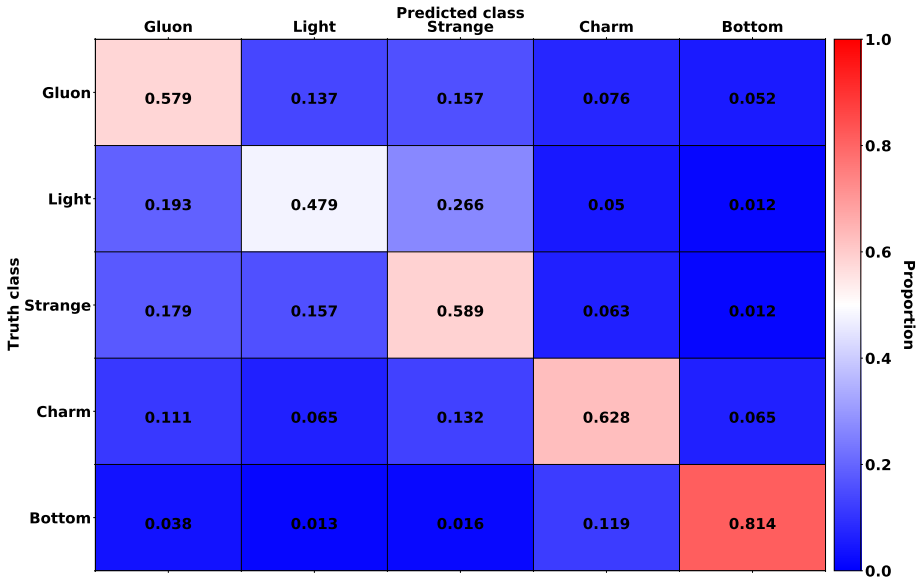

Figure 5: Confusion matrix for the output of the described jet flavour tagger, Eq. 5. Each truth class (i.e., row) is normalised to 1.

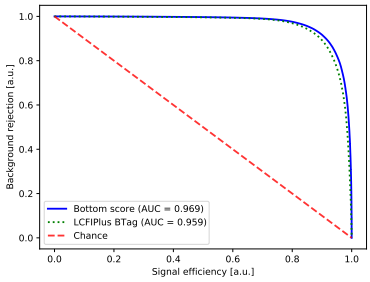

(a) b-jet score

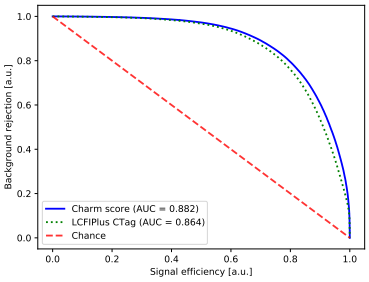

(b) c-jet score

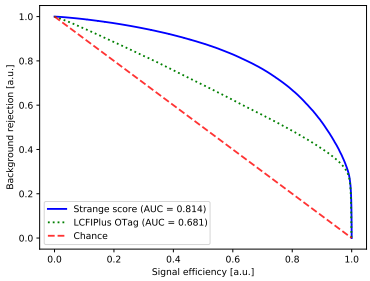

(c) s-jet score

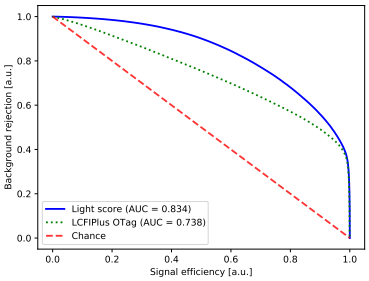

(d) u/d-jet score

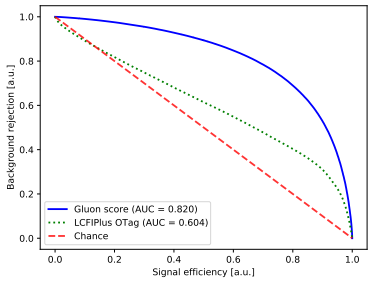

(e) g-jet score

Figure 6: ROC curves for each output node of the described jet flavour tagger, Eq. 5. Also shown on each graph is the ROC curve for the appropriate LFCIPlus tagger: "BTagger" for b-jet node, "CTagger" for c-jet node, and "OTagger" for light-, s-, and g-jet nodes. The area under the curve (AUC) is given for each tagger – ideally, AUC = 1 (i.e., 100% background rejection with 100% signal efficiency).

5 Higgs to strange analysis

The jet flavour tagger described in Section 4 is applied to a search for SM Higgs decaying to strange quarks ($h \to s\bar{s}$), using all of the MC samples described in Table 2. The parameter of interest (POI) for the analysis is the Higgs-strange quark coupling strength modifier, κ_s, which tunes the SM $h \to s\bar{s}$ BR, $\text{BR}[h \to s\bar{s}]_{\text{SM}}$, as:

$$\text{BR}[h \to s\bar{s}] = \mu(\kappa_s) \times \text{BR}[h \to s\bar{s}]_{\text{SM}} \,, \tag{6}$$

where $\text{BR}[h \to s\bar{s}]$ is the modified BR and $\mu(\kappa_s)$ is our POI as a function of κ_s, given by[2]:

$$\mu(\kappa_s) = \frac{\kappa_s^2}{\kappa_s^2 \times \text{BR}[h \to s\bar{s}]_{\text{SM}} + (1 - \text{BR}[h \to s\bar{s}]_{\text{SM}})} \,. \tag{7}$$

The coupling strength modifier is understood within the context of the kappa framework, the experimental tool for exploring the properties of the Higgs [47, 48]. When $\kappa_s = 1$, the SM BR is recovered.

5.1 Kinematic selections

The measurement of $h \to s\bar{s}$ is performed using the associated production mode in two channels based on the decay of the Z: $Z \to \nu\bar{\nu}$ and $Z \to \ell\ell$. The kinematic selections for each channel, detailed in Table 3, are designed to be orthogonal and to reduce the dominant Z, VV, and $h \to b\bar{b}/c\bar{c}/gg$ backgrounds. The cuts on the number of PFOs per event and per jet reduce the $h \to gg$ backgrounds – in general, gluon jets have a higher track multiplicity than quark jets. N.B. the $h(\to s\bar{s})Z(\to \nu\bar{\nu})$ and $h(\to s\bar{s})Z(\to \ell\ell)$ are combined to define the signal template for both channels (with orthogonality applied via the object counting cuts).

The cutflow for the $Z \to \nu\bar{\nu}$ channel is shown in Table 4. Histograms of the variables included as part of this channel's selections (showing the evolution of the yields as previous selection are applied) are shown in Figures 7 and 8.

From Table 4, we see the signal efficiency for our selections is 14% while our background efficiency is 0.005%. Even with the high background rejection, $Z \to q\bar{q}$ is still highly dominant with ∼16,000 events compared to the ∼9 events expected for $h \to s\bar{s}$. Therefore, improvements to the sensitivity of the analysis are expected to be accompanied by improved rejection of $Z \to q\bar{q}$. The $h \to gg$ process is the dominant Higgs background with ∼400 events.

The cutflow for the $Z \to \ell\ell$ channel is shown in Table 5. Histograms of the variables included as part of this channel's selections (showing the evolution of the yields as previous selection are applied) are shown in Figures 9, 10, and 11.

From Table 5, the hadronic backgrounds are almost entirely removed by cutting on the number of leptons. The signal efficiency for our selections is 7% while our background efficiency is 0.002%. The $4f$ single Z and ZZ backgrounds

[2] The POI has the same form as that used by ATLAS for measuring the Higgs-charm quark coupling strength modifier – for instance, see Eq. 1 of Ref. [46].

[3] "SFOS" stands for "same-flavour, opposite-sign".

[4] $\Delta R \equiv \sqrt{\Delta\eta^2 + \Delta\phi^2}$.

[5] If the 4-vectors of jets summed to ($\sqrt{s}$, 0, 0, 0), then $\Delta R_{jj,\text{miss}} = \pi$ – the fact that this isn't true implies there are additional PFOs/tracks in the event not grouped into either jet.

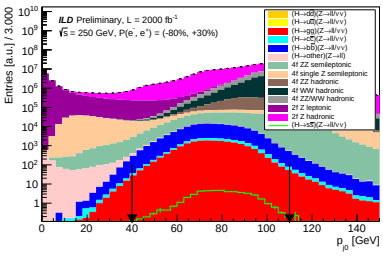

(a) Leading jet momentum p_{j_0}

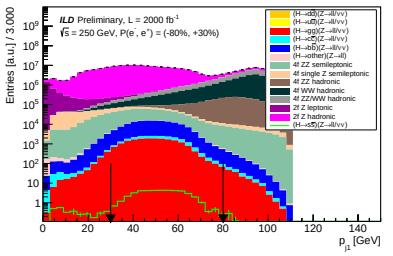

(b) Subleading jet momentum p_{j_1}

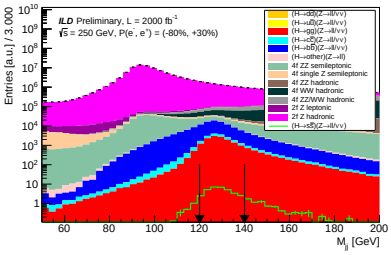

(c) Dijet mass M_{jj}

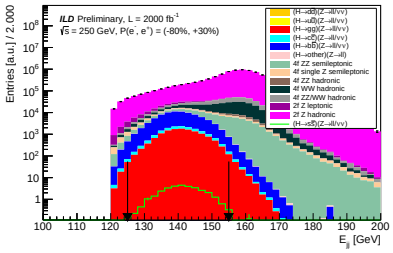

(d) Dijet energy E_{jj}

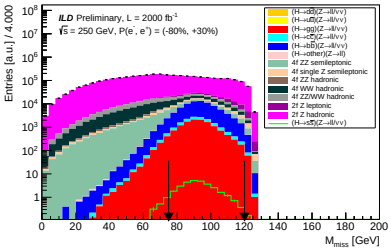

(e) Missing mass M_{miss}

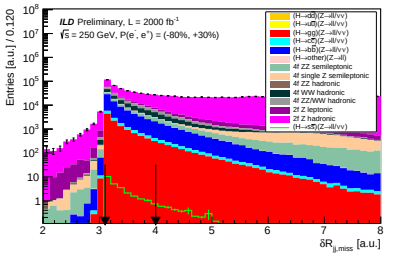

(f) Angular separation $\Delta R_{jj,\text{miss}}$

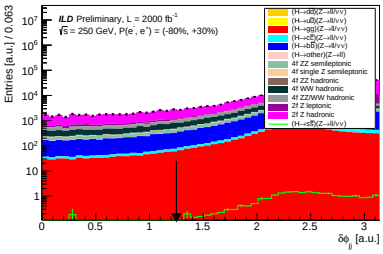

(g) Dijet azimuthal separation $\Delta\phi_{jj}$

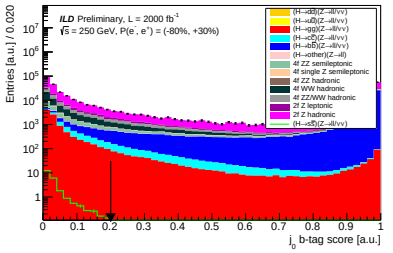

(h) Leading jet BTag score

Figure 7: Histograms of the variables used in the kinematic selections of the $Z \to \nu\bar{\nu}$ channel, as described in Table 3. Each histogram is given at the level of its corresponding selection but *before* that selection is applied. The arrows represent the placement of the selection cuts, and the error bars represent the Poisson counting uncertainties on those yields. The sum-of-weights per process is normalised to the SM cross-section. N.B. the $h(\to s\bar{s})Z(\to \ell\ell/\nu\bar{\nu})$ signal is unstacked.

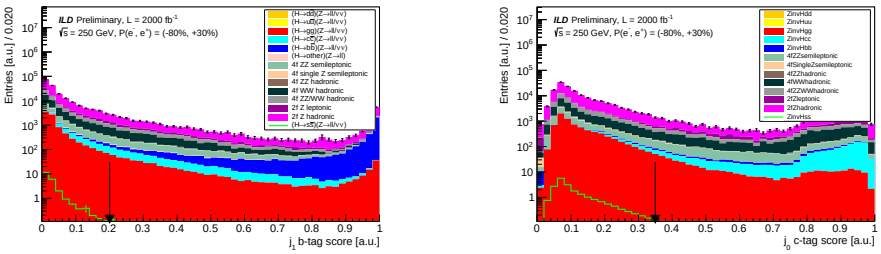

(a) Subleading jet BTag score

(b) Leading jet CTag score

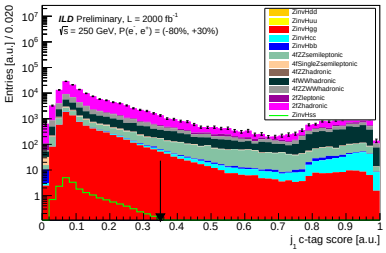

(c) Subleading jet CTag score

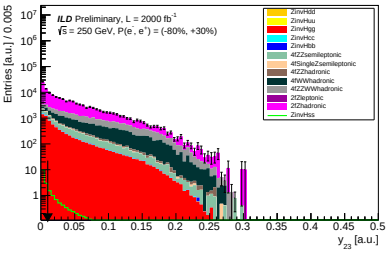

(d) $2 \to 3$ jet transition variable y_{23}

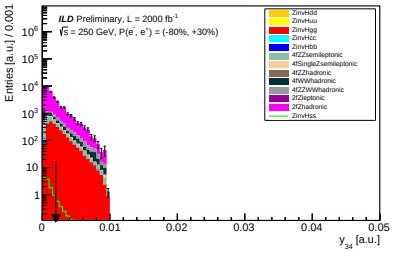

(e) $3 \to 4$ jet transition variable y_{34}

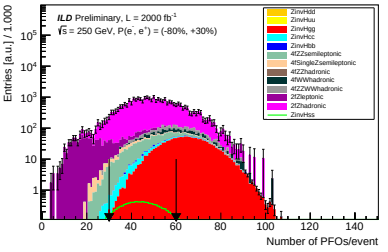

(f) Number of PFOs in event

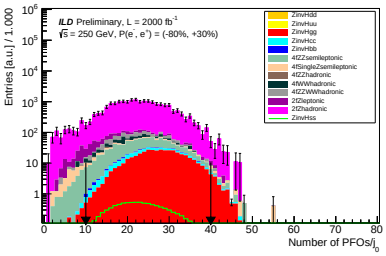

(g) Number of PFOs in leading jet

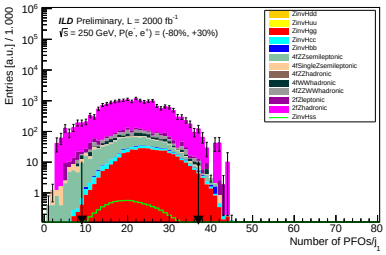

(h) Number of PFOs in subleading jet

Figure 8: Histograms of the variables used in the kinematic selections of the $Z \to \nu\bar{\nu}$ channel, as described in Table 3. Each histogram is given at the level of its corresponding selection but *before* that selection is applied. The arrows represent the placement of the selection cuts, and the error bars represent the Poisson counting uncertainties on those yields. The sum-of-weights per process is normalised to the SM cross-section. N.B. the $h(\to s\bar{s})Z(\to \ell\ell/\nu\bar{\nu})$ signal is unstacked. A continuation of Figure 7.

Table 3: Kinematic selections for $Z \to \nu\bar{\nu}$ and $Z \to \ell\ell$ channels of the $h \to s\bar{s}$ analysis. The selections are grouped into categories serving specific purposes.

Category	Selection	$Z \to \nu\bar{\nu}$	$Z \to \ell\ell$
Object counting	Number of leptons, N_{leptons}	0	≥ 2
	Number of jets, N_{jets}	≥ 2	≥ 2
	Leading 2 leptons are SFOS[3]	–	True
$2f$ Z rejection	Leading jet momentum, p_{j_0}	$\in [40, 110]$ GeV	$\in [60, 110]$ GeV
	Subleading jet momentum, p_{j_1}	$\in [30, 80]$ GeV	$\in [30, 75]$ GeV
	Dijet mass, M_{jj}	$\in [120, 140]$ GeV	$\in [115, 145]$ GeV
	Dijet energy, E_{jj}	$\in [125, 155]$ GeV	$\in [130, 160]$ GeV
	Missing mass, M_{miss}	$\in [75, 120]$ GeV	–
	Dijet/missing-p^{μ} angular separation, $\Delta R_{jj,\text{miss}}$[4]	$\in [3.1, 4.0]$[5]	–
	Dijet azimuthal separation, $\Delta\phi_{jj}$	> 1.25	> 1.75
	Leading lepton momentum, p_{ℓ_0}	–	$\in [40, 90]$ GeV
	Subleading lepton momentum, p_{ℓ_1}	–	$\in [20, 60]$ GeV
	Dilepton mass, $M_{\ell\ell}$	–	$\in [70, 100]$ GeV
	Dilepton energy, $E_{\ell\ell}$	–	$\in [85, 115]$ GeV
$h \to b\bar{b}/c\bar{c}$ rejection	Leading jet LCFIPlus BTag score, $\text{score}_b^{j_0}$	< 0.20	< 0.1
	Subleading jet LCFIPlus BTag score, $\text{score}_b^{j_1}$	< 0.20	< 0.1
	Leading jet LCFIPlus CTag score, $\text{score}_c^{j_0}$	< 0.35	< 0.3
	Subleading jet LCFIPlus CTag score, $\text{score}_c^{j_1}$	< 0.35	< 0.3
$4f$ VV rejection	$2 \to 3$ jet transition variable, y_{23}	< 0.010	< 0.050
	$3 \to 4$ jet transition variable, y_{34}	< 0.002	< 0.005
$h \to gg$ rejection	Number of PFOs in event, $N_{\text{PFOs}}^{\text{event}}$	$\in [30, 60]$	$\in [20, 80]$
	Number of PFOs in leading jet, $N_{\text{PFOs}}^{j_0}$	$\in [10, 40]$	$\in [5, 50]$
	Number of PFOs in subleading jet, $N_{\text{PFOs}}^{j_1}$	$\in [9, 37]$	$\in [5, 50]$

are the dominant backgrounds, with ∼7,000 events compared to the ∼4 events expected for $h \to s\bar{s}$. As with the $Z \to \nu\bar{\nu}$ channel, the $h \to gg$ process is the dominant Higgs background with ∼700 events.

5.2 Limits on Higgs-strange coupling strength modifier

The estimated significance of discovery, $Z_0 \approx s/\sqrt{b}$, using the signal and background yields at the level of the last selection in Table 3 is $\sim 0.1\sigma$. Therefore, a discovery measurement of $h \to s\bar{s}$ is *unlikely*, given the use of a best-case jet flavour tagger. However, limits on κ_s, and accordingly $\text{BR}[h \to s\bar{s}]$, may be set instead, allowing to reduce the phase space for BSM enhancements to the $h \to s\bar{s}$ rate.

The chosen fit discriminant for $h \to s\bar{s}$ is the sum of strange jet tagger scores for the leading and subleading momentum jets, using the jet flavour tagger described in Section 4, as shown in Figure 12. A higher sum of scores corresponds to a higher probability of an event containing an $s\bar{s}$ system.

The fitted likelihood is a simple Poisson probability density function (PDF):

$$L(\kappa_s\,;\,\vec{n},\vec{s},\vec{b}) = \prod_{i=1}^{N} \frac{(\mu(\kappa_s) \times s_i + b_i)^n \times \exp(\mu(\kappa_s) \times s_i + b_i)}{n_i!}\,, \tag{8}$$

where our POI, $\mu(\kappa_s)$, is given by Eq. 7, $\vec{s}$ is the vector of expected signal yields (in N bins – $s_i \in [\vec{s}]_i$ is the expected signal yield in i-th bin), $\vec{b}$ is the vector of expected background yields, and $\vec{n}$ is the vector of observed yields. As observed yields are unavailable, "Asimov" [49] data is assumed. The Python package `pyhf` [50, 51] is used to set the limits.

Table 4: Cutflow for the $Z \to \nu\bar{\nu}$ channel selections described in Table 3. Shown are the central values in the yields as well as the Poisson counting uncertainties on those yields. The signal (background) efficiency is defined as the ratio of the $h(\to s\bar{s})Z(\to \ell\ell/\nu\bar{\nu})$ (all non-$h(\to s\bar{s})Z(\to \ell\ell/\nu\bar{\nu})$) yields at a given cut value to the yields at "No cut". The sum-of-weights per process is normalised to the SM cross-section.

ILD Preliminary, $\mathcal{L} = 2000$ fb^{-1}, $\sqrt{s} = 250$ GeV, $P(e^-, e^+) = (-80\%, +30\%)$

	$(H \to s\bar{s})(Z \to \ell\ell/\nu\nu)$	$(H \to gg)(Z \to \ell\ell/\nu\nu)$	$(H \to u\bar{u}/d\bar{d})(Z \to b\bar{b}/\nu\nu)$	$(H \to c\bar{c})(Z \to \ell\ell/\nu\nu)$	$(H \to b\bar{b})(Z \to \ell\ell/\nu\nu)$	$(H \to \text{other})(Z \to \ell\ell)$	$2f$ Z hadronic	$4f$ ZZ hadronic	$4f$ WW hadronic	$4f$ ZZ/WW hadronic	$2f$ Z leptonic	$4f$ ZZ semileptonic	$4f$ single Z semileptonic	Total bkg.	Sig. eff.	Bkg. eff.
No cut	64.51 ± 1.14	26095.47 ± 35.08	0.13 ± 0.0	8860.89 ± 16.64	175695.3 ± 176.22	31773.76 ± 46.82	$2559310\,62.5 \pm 50827.22$	$2810\,19.87 \pm 1054.69$	$2973\,2839.84 \pm 7731.14$	$2417\,7280.41 \pm 5691.47$	$4242\,8033.91 \pm 8571.75$	$1676\,158.94 \pm 817.92$	$2539\,817.83 \pm 1016.32$	$3595\,37773.37 \pm 52458.49$	1.00e+00	1.00e+00
No leptons	48.29 ± 0.6	19695.06 ± 27.73	0.13 ± 0.0	6675.43 ± 11.18	$131\,811.89 \pm 167.15$	6268.25 ± 20.66	$2530\,924\,2.95 \pm 50604.44$	$2795\,922.02 \pm 1052.03$	$2960\,4798.82 \pm 7714.47$	$2407\,3642.64 \pm 5679.26$	$1872\,17\,39.44 \pm 5693.99$	$851\,521.55 \pm 582.98$	$1011\,752.12 \pm 641.45$	$3309\,16318.59 \pm 51835.17$	7.40e-01	9.20e-01
≥ 2 jets	48.29 ± 0.6	19695.06 ± 27.73	0.13 ± 0.0	6675.43 ± 11.18	$131\,811.89 \pm 167.15$	6216.23 ± 20.58	$2530\,923\,1.92 \pm 50604.43$	$2795\,922.02 \pm 1052.03$	$2960\,4798.82 \pm 7714.47$	$2407\,3642.64 \pm 5679.26$	$1780\,382.5 \pm 5556.78$	$851\,521.55 \pm 582.98$	$1011\,750.09 \pm 641.45$	$3300\,24796.57 \pm 51820.27$	7.40e-01	9.18e-01
$p_{j_1} \in [40, 110]$ GeV	47.41 ± 0.59	19512.14 ± 27.58	0.13 ± 0.0	6591.48 ± 11.07	$130\,386.65 \pm 166.35$	4719.6 ± 17.93	$1574\,98\,040.21 \pm 39872.4$	$2508\,108.58 \pm 996.41$	$2539\,4290.9 \pm 7144.85$	$2072\,0712.03 \pm 5268.93$	$397\,3417.2 \pm 2623.16$	$689\,124.99 \pm 524.45$	$407\,773.91 \pm 407.23$	$2113\,52725.23 \pm 40950.73$	7.35e-01	5.88e-01
$p_{j_2} \in [30, 80]$ GeV	43.65 ± 0.54	18516.51 ± 26.82	0.12 ± 0.0	6286.23 ± 10.71	$122\,931.01 \pm 161.78$	3704.24 ± 15.88	$1072878\,81.34 \pm 32908.66$	$1005\,428.35 \pm 630.87$	6139566.28 ± 3513.13	5224597.83 ± 2645.74	$522\,979.7 \pm 951.67$	$508\,522.82 \pm 450.51$	$150\,690.35 \pm 247.55$	$1\,209\,91\,148.43 \pm 33225.25$	6.77e-01	3.37e-01
$M_{jj} \in [120, 140]$ GeV	32.05 ± 0.38	13381.62 ± 22.26	0.09 ± 0.0	4197.13 ± 8.2	$69\,510.76 \pm 123.28$	1176.03 ± 8.95	$847\,1\,483.31 \pm 9247.29$	$160\,96.34 \pm 79.82$	$217\,86.18 \pm 660.01$	$174\,691.55 \pm 483.79$	$5098.2\,87 \pm 297.14$	$71\,310.19 \pm 168.71$	$19\,882.33 \pm 89.92$	$9\,110\,030.46 \pm 9291.41$	4.97e-01	2.53e-02
$E_{jj} \in [125, 155]$ GeV	31.54 ± 0.37	13195.22 ± 22.09	0.09 ± 0.0	4138.2 ± 8.13	$68\,431.89 \pm 122.37$	1130.0 ± 8.77	$31\,15\,326.57 \pm 5607.72$	8724.87 ± 58.77	$103\,011.37 \pm 455.06$	$831\,33.43 \pm 333.74$	$45\,493.21 \pm 280.68$	$44\,520.23 \pm 133.3$	$15\,399.87 \pm 79.14$	$350\,25\,36.49 \pm 56\,46.85$	4.89e-01	9.74e-03
$M_{\text{miss}} \in [75, 120]$ GeV	29.66 ± 0.36	12431.98 ± 21.42	0.09 ± 0.0	3897.6 ± 7.86	$64\,672.67 \pm 119.07$	1014.35 ± 8.31	$1\,249\,359.28 \pm 3579.54$	4371.34 ± 41.6	$46\,621.77 \pm 306.14$	$37\,363.09 \pm 223.74$	$36\,735.72 \pm 252.22$	$24\,247.55 \pm 98.38$	$11\,056.09 \pm 67.05$	$1\,51\,1801.18 \pm 3612.64$	4.60e-01	4.20e-03
$\Delta R_{jj,\text{miss}} \in [3.1, 4.0]$	25.27 ± 0.31	10708.0 ± 19.88	0.07 ± 0.0	3358.7 ± 7.3	$55\,705.28 \pm 110.51$	866.91 ± 7.68	$212\,330.4 \pm 1464.0$	3092.75 ± 34.99	$366\,83.09 \pm 271.56$	$29\,230.48 \pm 197.9$	$15\,476.7 \pm 163.71$	$15\,023.41 \pm 77.44$	881.28 ± 18.93	$383\,382.34 \pm 1517.66$	3.92e-01	1.07e-03
$\Delta\phi_{jj} > 1.25$	23.84 ± 0.31	9939.25 ± 19.15	0.07 ± 0.0	3163.72 ± 7.08	$52\,405.74 \pm 107.21$	779.39 ± 7.28	$190\,315.06 \pm 1386.03$	2789.54 ± 33.23	$325\,43.98 \pm 255.78$	25899.73 ± 186.28	$13\,228.88 \pm 151.36$	$13\,633.66 \pm 73.77$	749.11 ± 17.45	$345\,471.96 \pm 1436.28$	3.70e-01	9.61e-04
$\text{score}_{\text{bkg}}^{0} < 0.20$	23.07 ± 0.31	9064.62 ± 18.28	0.07 ± 0.0	$2\,455.55 \pm 6.2$	4481.42 ± 31.41	601.51 ± 6.4	$127\,610.22 \pm 1134.95$	1554.49 ± 24.81	$280\,47.04 \pm 237.45$	22362.65 ± 173.09	8958.37 ± 124.55	9276.43 ± 60.85	621.41 ± 15.9	$2\,15056.84 \pm 1181.5$	3.58e-01	5.98e-04
$\text{score}_{\text{bkg}}^{1} < 0.20$	22.26 ± 0.3	8505.84 ± 17.7	0.07 ± 0.0	1920.09 ± 5.46	477.27 ± 10.28	493.89 ± 5.8	$111\,106.29 \pm 1059.02$	1259.98 ± 22.33	$24\,117.0 \pm 220.18$	19759.41 ± 162.71	6572.01 ± 106.68	7567.38 ± 54.96	541.7 ± 14.84	182343.2 ± 1100.95	3.45e-01	5.07e-04
$\text{score}_{\text{bkg}}^{0} < 0.35$	21.34 ± 0.28	8037.73 ± 17.19	0.06 ± 0.0	681.96 ± 3.26	245.28 ± 7.36	370.8 ± 5.02	$956\,42.05 \pm 982.56$	1077.1 ± 20.65	18413.91 ± 192.4	16643.03 ± 149.33	2673.83 ± 68.05	5892.26 ± 48.49	492.49 ± 14.15	$150\,191.86 \pm 1016.24$	3.31e-01	4.18e-04
$\text{score}_{\text{bkg}}^{1} < 0.35$	20.61 ± 0.27	7627.12 ± 16.73	0.06 ± 0.0	279.98 ± 2.07	139.46 ± 5.56	281.77 ± 4.38	87597.02 ± 940.33	974.58 ± 19.64	13237.51 ± 163.13	14368.05 ± 138.75	1451.21 ± 50.13	4338.87 ± 41.61	447.76 ± 13.49	$130\,764.01 \pm 967.07$	3.20e-01	3.64e-04
$y_{23} < 0.010$	13.45 ± 0.23	2783.47 ± 10.11	0.04 ± 0.0	157.85 ± 1.53	59.82 ± 3.65	9.74 ± 0.81	31443.27 ± 563.38	113.61 ± 6.71	1055.38 ± 46.06	1302.29 ± 41.77	1314.4 ± 47.71	1130.72 ± 21.24	165.52 ± 8.2	$395\,49.56 \pm 569.4$	2.08e-01	1.10e-04
$y_{34} < 0.002$	11.64 ± 0.22	1508.06 ± 7.44	0.03 ± 0.0	128.67 ± 1.39	42.88 ± 3.1	2.32 ± 0.4	24306.71 ± 495.33	47.11 ± 4.32	492.51 ± 31.47	637.75 ± 29.23	1286.69 ± 47.2	806.23 ± 17.94	122.82 ± 7.07	29393.42 ± 499.89	1.80e-01	8.17e-05
$N_{\text{PFOs}}^{\text{cent}} \in [30, 60]$	9.71 ± 0.19	460.46 ± 4.07	0.03 ± 0.0	96.57 ± 1.18	21.42 ± 2.2	1.23 ± 0.29	18351.16 ± 430.39	21.38 ± 2.91	241.23 ± 22.02	337.63 ± 21.27	438.13 ± 27.55	619.44 ± 15.72	95.16 ± 6.22	20693.55 ± 432.73	1.50e-01	5.75e-05
$N_{\text{PFOs}}^{\text{fwd}} \in [10, 40]$	9.44 ± 0.19	445.06 ± 4.0	0.03 ± 0.0	94.58 ± 1.17	21.19 ± 2.19	1.23 ± 0.29	$171\,49.96 \pm 416.07$	20.58 ± 2.85	233.19 ± 21.65	329.59 ± 21.01	349.81 ± 24.61	591.5 ± 15.36	69.95 ± 5.33	19316.11 ± 418.24	1.46e-01	5.37e-05
$N_{\text{PFOs}} \in [9, 37]$	9.15 ± 0.19	431.49 ± 3.94	0.03 ± 0.0	92.25 ± 1.16	19.56 ± 2.1	1.23 ± 0.29	$161\,00.17 \pm 403.13$	20.19 ± 2.83	223.14 ± 21.18	324.23 ± 20.84	309.98 ± 23.17	559.17 ± 14.94	57.34 ± 4.83	$18\,147.92 \pm 405.23$	1.42e-01	5.05e-05

Table 5: Cutflow for the $Z \to \ell\ell$ channel selections described in Table 3. Shown are the central values in the yields as well as the Poisson counting uncertainties on those yields. The signal (background) efficiency is defined as the ratio of the $h(\to s\bar{s})Z(\to \ell\ell/\nu\bar{\nu})$ (all non-$h(\to s\bar{s})Z(\to \ell\ell/\nu\bar{\nu})$) yields at a given cut value to the yields at "No cut". The sum-of-weights per process is normalised to the SM cross-section.

ILD Preliminary, $\mathcal{L} = 2000$ fb^{-1}, $\sqrt{s} = 250$ GeV, $P(e^-, e^+) = (-80\%, +30\%)$

	$(H \to s\bar{s})(Z \to \ell\ell/\nu\nu)$	$(H \to gg)(Z \to \ell\ell/\nu\nu)$	$(H \to u\bar{u}/d\bar{d})(Z \to \ell\ell/\nu\nu)$	$(H \to c\bar{c})(Z \to \ell\ell/\nu\nu)$	$(H \to b\bar{b})(Z \to \ell\ell/\nu\nu)$	$(H \to \text{other})(Z \to \ell\ell)$	$2f$ Z hadronic	$4f$ ZZ hadronic	$4f$ WW hadronic	$4f$ ZZ/WW hadronic	$2f$ Z leptonic	$4f$ ZZ semileptonic	$4f$ single Z semileptonic	Total bkg.	Sig. eff.	Bkg. eff.
No cut	64.51 ± 1.14	26095.47 ± 35.08	0.13 ± 0.0	8860.89 ± 16.64	175695.3 ± 176.22	31773.76 ± 46.82	25593102.5 ± 50827.22	2810119.87 ± 1054.69	29732839.84 ± 7731.14	24177280.41 ± 5691.47	4242803.91 ± 857.75	1676158.94 ± 817.92	2539817.83 ± 1016.32	$359537773.37 \pm 52458.49$	1.00e+00	1.00e+00
≥ 2 leptons	12.55 ± 0.86	5094.72 ± 19.19	0.0 ± 0.0	1725.93 ± 10.98	34414.35 ± 48.59	20045.48 ± 37.27	19713.87 ± 446.09	87.09 ± 5.87	800.08 ± 40.1	625.69 ± 28.95	1703473.21 ± 557.302	425681.95 ± 412.19	599633.62 ± 493.82	1904259.54 ± 5028.32	1.95e-01	5.30e-02
Leading 2 leptons are SFOS	12.22 ± 0.85	5029.16 ± 19.06	0.0 ± 0.0	1703.55 ± 10.9	33915.11 ± 48.24	17026.98 ± 34.35	11870.72 ± 346.16	55.02 ± 4.67	482.46 ± 31.14	353.71 ± 21.77	1708306.61 ± 5533.92	420043.13 ± 409.45	573238.66 ± 482.83	1874766732 ± 5581.25	1.89e-01	5.21e-02
≥ 2 jets	12.22 ± 0.85	5029.16 ± 19.06	0.0 ± 0.0	1703.55 ± 10.9	33915.11 ± 48.24	16930.03 ± 34.25	11870.72 ± 346.16	55.02 ± 4.67	482.46 ± 31.14	353.71 ± 21.77	1668872.84 ± 5375.94	420043.13 ± 409.45	573238.66 ± 482.83	1775235661 ± 5424.65	1.89e-01	4.94e-02
$p_{j_0} \in [60, 110]$ GeV	11.95 ± 0.84	4571.55 ± 18.17	0.0 ± 0.0	1595.44 ± 10.55	30236.02 ± 45.55	6539.54 ± 21.29	6308.84 ± 252.35	46.71 ± 4.3	379.94 ± 27.64	285.38 ± 19.55	235006.12 ± 637.94	344790.79 ± 370.96	385873.61 ± 396.14	1015645.88 ± 877.12	1.85e-01	2.82e-03
$p_{j_1} \in [30, 75]$ GeV	11.5 ± 0.82	4375.06 ± 17.78	0.0 ± 0.0	1538.03 ± 10.36	28689.22 ± 44.37	5140.28 ± 18.88	3664.18 ± 192.32	17.81 ± 2.66	104.53 ± 14.5	66.99 ± 9.47	10650.29 ± 135.81	23365.14 ± 305.06	243602.82 ± 314.75	531025.84 ± 500.62	1.78e-01	1.48e-03
$M_{jj} \in [115, 145]$ GeV	9.81 ± 0.76	3691.65 ± 16.32	0.0 ± 0.0	1264.68 ± 9.39	22453.12 ± 39.25	3706.97 ± 16.03	504.71 ± 71.38	1.19 ± 0.69	6.03 ± 3.48	5.36 ± 2.68	2658.24 ± 67.85	41899.98 ± 129.32	61397.77 ± 158.02	137599.51 ± 231.44	1.52e-01	3.83e-04
$E_{jj} \in [130, 160]$ GeV	9.63 ± 0.75	3546.02 ± 16.0	0.0 ± 0.0	1182.85 ± 9.09	20125.91 ± 37.16	3513.65 ± 15.6	363.39 ± 60.56	1.19 ± 0.69	6.03 ± 3.48	4.02 ± 2.32	1948.22 ± 58.08	35688.82 ± 119.35	52414.55 ± 146.0	118804.28 ± 211.15	1.49e-01	3.30e-04
$\Delta\phi_{jj} > 1.75$	8.33 ± 0.7	3122.06 ± 15.01	0.0 ± 0.0	1066.59 ± 8.63	18087.03 ± 35.23	2964.88 ± 14.33	312.92 ± 56.2	1.19 ± 0.69	2.01 ± 2.01	2.68 ± 1.89	1078.88 ± 43.22	27193.48 ± 104.18	41553.26 ± 130.0	95393.31 ± 185.84	1.29e-01	2.65e-04
$p_{l_0} \in [40, 90]$ GeV	8.28 ± 0.7	3083.46 ± 14.92	0.0 ± 0.0	1053.16 ± 8.57	17864.64 ± 35.01	2923.97 ± 14.23	80.75 ± 28.55	0.4 ± 0.4	0.0 ± 0.0	0.0 ± 0.0	464.11 ± 28.35	23032.62 ± 95.88	34281.36 ± 118.07	82792.75 ± 162.72	1.28e-01	2.30e-04
$p_{l_1} \in [20, 60]$ GeV	8.23 ± 0.7	3033.43 ± 14.8	0.0 ± 0.0	1034.14 ± 8.5	17531.96 ± 34.68	2874.49 ± 14.11	60.56 ± 24.73	0.0 ± 0.0	0.0 ± 0.0	0.0 ± 0.0	349.81 ± 24.61	21456.08 ± 92.54	29059.81 ± 109.83	76008.52 ± 153.42	1.28e-01	2.11e-04
$M_H \in [70, 100]$ GeV	7.71 ± 0.67	2871.04 ± 14.39	0.0 ± 0.0	978.1 ± 8.26	16618.67 ± 33.76	2726.42 ± 13.74	40.38 ± 20.19	0.0 ± 0.0	0.0 ± 0.0	0.0 ± 0.0	296.13 ± 22.65	16918.05 ± 82.17	21311.83 ± 93.1	61768.32 ± 133.96	1.20e-01	1.72e-04
$E_H \in [85, 115]$ GeV	7.66 ± 0.67	2843.63 ± 14.32	0.0 ± 0.0	967.53 ± 8.22	16436.56 ± 33.57	2694.88 ± 13.66	40.38 ± 20.19	0.0 ± 0.0	0.0 ± 0.0	0.0 ± 0.0	162.78 ± 16.79	10095.83 ± 63.48	14714.61 ± 77.36	47963.86 ± 110.86	1.19e-01	1.33e-04
score$^{\nu\bar{\nu}}_{\nu\bar{\nu}q\bar{q}} < 0.1$	6.74 ± 0.63	2435.67 ± 13.26	0.0 ± 0.0	570.02 ± 6.31	810.59 ± 7.45	1883.22 ± 11.42	30.28 ± 17.48	0.0 ± 0.0	0.0 ± 0.0	0.0 ± 0.0	133.35 ± 15.2	709.62 ± 53.21	10389.54 ± 65.0	23353.01 ± 89.41	1.04e-01	6.49e-05
score$^{l\bar{l}}_{\nu\bar{\nu}q\bar{q}} < 0.1$	6.08 ± 0.6	2145.87 ± 12.44	0.0 ± 0.0	332.25 ± 4.81	76.16 ± 2.28	1416.5 ± 9.9	20.19 ± 14.28	0.0 ± 0.0	0.0 ± 0.0	0.0 ± 0.0	105.64 ± 13.53	599.44 ± 48.91	8752.64 ± 59.66	18849.77 ± 81.37	9.43e-02	5.24e-05
score$^{\nu\bar{\nu}}_{l\bar{l}q\bar{q}} < 0.3$	5.96 ± 0.59	2055.37 ± 12.18	0.0 ± 0.0	129.61 ± 3.01	53.15 ± 1.91	1209.79 ± 9.15	20.19 ± 14.28	0.0 ± 0.0	0.0 ± 0.0	0.0 ± 0.0	100.44 ± 13.19	545.81 ± 46.68	8047.85 ± 57.21	17081.16 ± 77.94	9.23e-02	4.75e-05
score$^{l\bar{l}}_{l\bar{l}q\bar{q}} < 0.3$	5.79 ± 0.58	1972.93 ± 11.93	0.0 ± 0.0	60.36 ± 2.05	40.25 ± 1.66	1042.23 ± 8.5	20.19 ± 14.28	0.0 ± 0.0	0.0 ± 0.0	0.0 ± 0.0	96.98 ± 12.96	5126.74 ± 45.23	7591.15 ± 55.56	15956.63 ± 75.68	8.97e-02	4.44e-05
$y_{23} < 0.050$	5.49 ± 0.57	1623.21 ± 10.82	0.0 ± 0.0	53.38 ± 1.93	36.75 ± 1.59	512.04 ± 5.95	20.19 ± 14.28	0.0 ± 0.0	0.0 ± 0.0	0.0 ± 0.0	96.98 ± 12.96	4121.35 ± 40.56	6027.86 ± 49.51	12497.25 ± 68.02	8.51e-02	3.47e-05
$y_{34} < 0.005$	4.75 ± 0.53	1160.13 ± 9.15	0.0 ± 0.0	46.48 ± 1.8	31.19 ± 1.46	119.85 ± 2.88	20.19 ± 14.28	0.0 ± 0.0	0.0 ± 0.0	0.0 ± 0.0	96.98 ± 12.96	3292.77 ± 36.25	4516.22 ± 42.86	9288.55 ± 60.17	7.36e-02	2.58e-05
$N^{\text{vismass}}_{\text{PFOs}} \in [20, 80]$	4.7 ± 0.53	755.14 ± 7.38	0.0 ± 0.0	43.81 ± 1.75	27.63 ± 1.38	99.07 ± 2.62	20.19 ± 14.28	0.0 ± 0.0	0.0 ± 0.0	0.0 ± 0.0	50.22 ± 9.33	3141.5 ± 35.41	4292.95 ± 41.78	8435.21 ± 57.94	7.28e-02	2.34e-05
$N^{E_T}_{\text{PFOs}} \in [5, 50]$	4.64 ± 0.52	722.43 ± 7.21	0.0 ± 0.0	42.9 ± 1.73	26.62 ± 1.35	94.92 ± 2.56	20.19 ± 14.28	0.0 ± 0.0	0.0 ± 0.0	0.0 ± 0.0	39.83 ± 8.31	3088.82 ± 35.11	4206.32 ± 41.36	8246.68 ± 57.27	7.26e-02	2.29e-05
$N^{\vec{p}}_{\text{PFOs}} \in [5, 50]$	4.64 ± 0.52	711.51 ± 7.16	0.0 ± 0.0	42.42 ± 1.72	26.41 ± 1.34	93.82 ± 2.55	20.19 ± 14.28	0.0 ± 0.0	0.0 ± 0.0	0.0 ± 0.0	39.83 ± 8.31	3056.09 ± 34.93	4160.37 ± 41.13	8155.28 ± 56.98	7.20e-02	2.27e-05

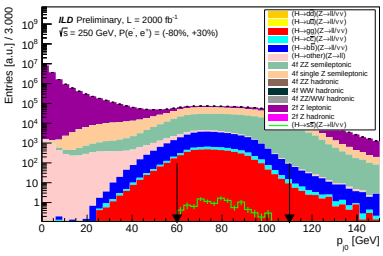

(a) Leading jet momentum p_{j_0}

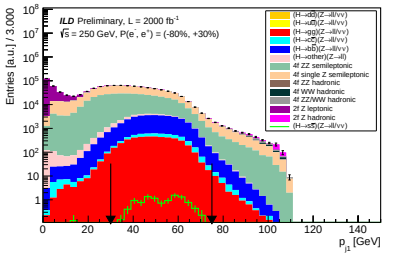

(b) Subleading jet momentum p_{j_1}

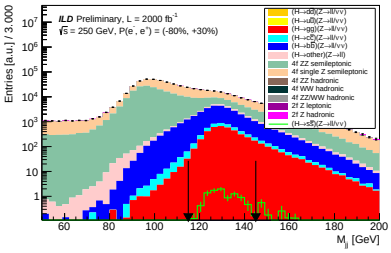

(c) Dijet mass M_{jj}

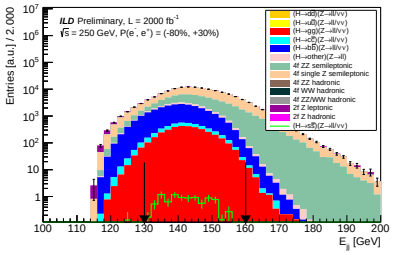

(d) Dijet energy E_{jj}

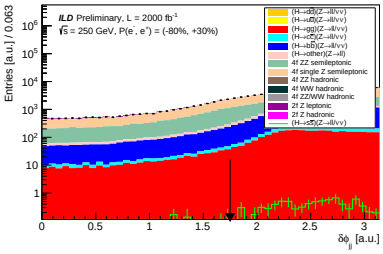

(e) Dijet azimuthal separation $\Delta\phi_{jj}$

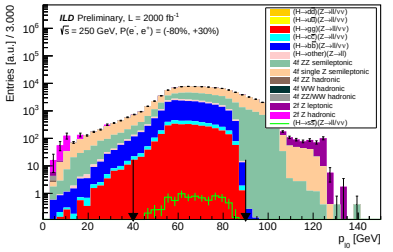

(f) Leading lepton momentum p_{ℓ_0}

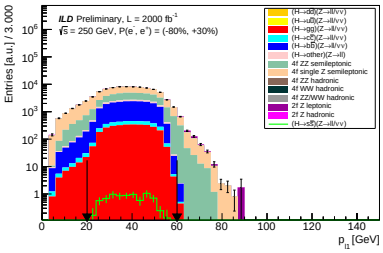

(g) Leading lepton momentum p_{ℓ_1}

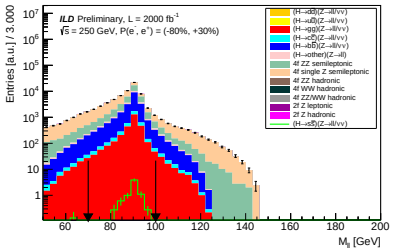

(h) Dilepton mass $M_{\ell\ell}$

Figure 9: Histograms of the variables used in the kinematic selections of the $Z \to \ell\ell$ channel, as described in Table 3. Each histogram is given at the level of its corresponding selection but *before* that selection is applied. The arrows represent the placement of the selection cuts, and the error bars represent the Poisson counting uncertainties on those yields. The sum-of-weights per process is normalised to the SM cross-section. N.B. the $h(\to s\bar{s})Z(\to \ell\ell/\nu\bar{\nu})$ signal is unstacked.

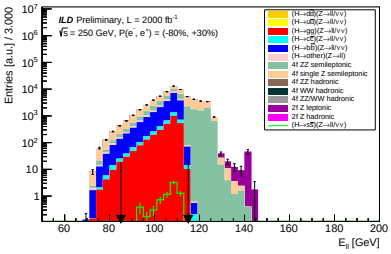

(a) Dilepton energy $E_{\ell\ell}$

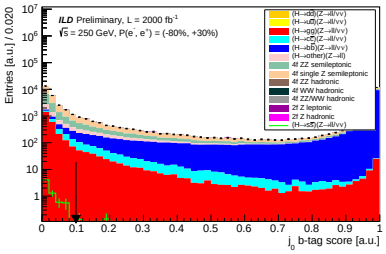

(b) Leading jet BTag score

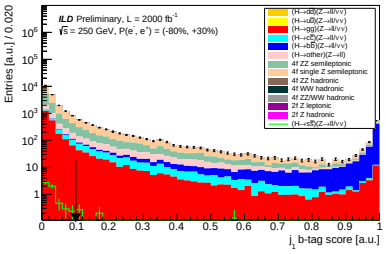

(c) Subleading jet BTag score

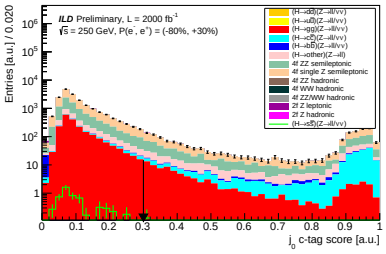

(d) Leading jet CTag score

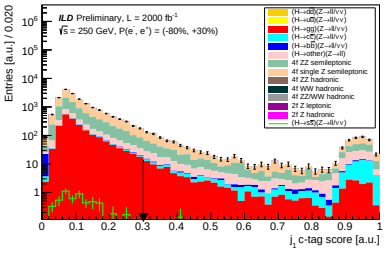

(e) Subleading jet CTag score

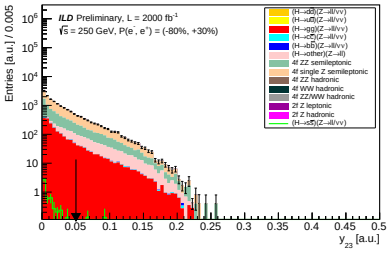

(f) $2 \to 3$ jet transition variable y_{23}

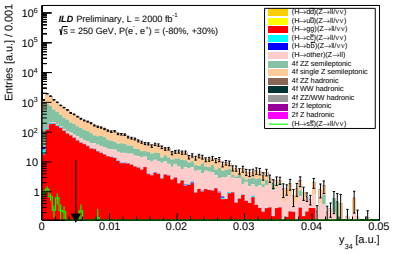

(g) $3 \to 4$ jet transition variable y_{34}

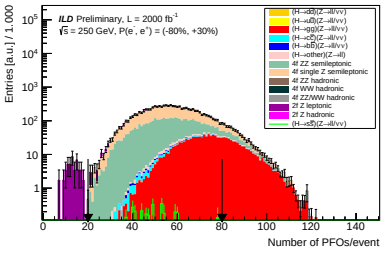

(h) Number of PFOs in event

Figure 10: Histograms of the variables used in the kinematic selections of the $Z \to \ell\ell$ channel, as described in Table 3. Each histogram is given at the level of its corresponding selection but *before* that selection is applied. The arrows represent the placement of the selection cuts, and the error bars represent the Poisson counting uncertainties on those yields. The sum-of-weights per process is normalised to the SM cross-section. N.B. the $h(\to s\bar{s})Z(\to \ell\ell/\nu\bar{\nu})$ signal is unstacked. A continuation of Figure 9.

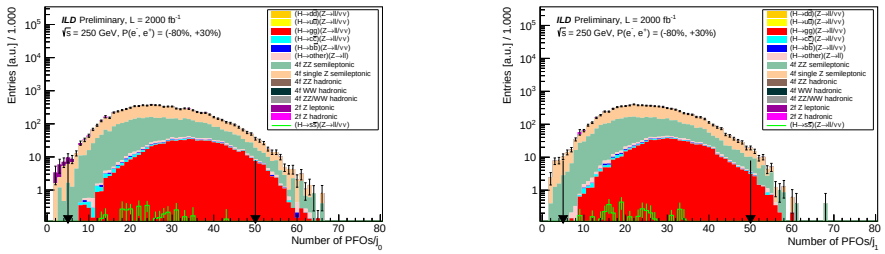

(a) Number of PFOs in leading jet

(b) Number of PFOs in subleading jet

Figure 11: Histograms of the variables used in the kinematic selections of the $Z \to \ell\ell$ channel, as described in Table 3. Each histogram is given at the level of its corresponding selection but *before* that selection is applied. The arrows represent the placement of the selection cuts, and the error bars represent the Poisson counting uncertainties on those yields. The sum-of-weights per process is normalised to the SM cross-section. N.B. the $h(\to s\bar{s})Z(\to \ell\ell/\nu\bar{\nu})$ signal is unstacked. A continuation of Figure 10.

Signal regions are built by requiring $0.5\times(\text{score}^s_{j_0}+\text{score}^s_{j_1})$ to be greater than some threshold – these thresholds are chosen such that the best (i.e., strongest) 95% CL_s upper limits [52] are obtained for the $Z \to \nu\bar{\nu}$ and $Z \to \ell\ell$ channels independently. Scans on the choice of threshold are shown in Figure. 13, which are found to be 0.35 and 0.40 for the $Z \to \nu\bar{\nu}$ and $Z \to \ell\ell$ channels, respectively, a trade-off between reducing the dominant backgrounds and the finiteness of MC statistics. The resulting limit plots on κ_s for these particular thresholds are shown in Figure 14, including both the single-channel and combined results.

From Figure 14, the 95% upper confidence bound on κ_s is found to be 8.97 for the $Z \to \nu\bar{\nu}$ channel and 6.28 for the $Z \to \ell\ell$ channel, leading to a combined limit of 5.95. This number is comparable to what has been estimated for the ILC (all data, $\sqrt{s} = 250\,\text{GeV}$ as well as $\sqrt{s} = 500\,\text{GeV}$) from other studies [53] using indirect measurements, $\kappa_s \lesssim 10$ at 95% confidence level (CL). However, the study here includes only two measurement channels and approximately 50% of the expected dataset for ILD. The limits are therefore expected to improve even more. [**TODO: other comparisons, discussion, etc.**]

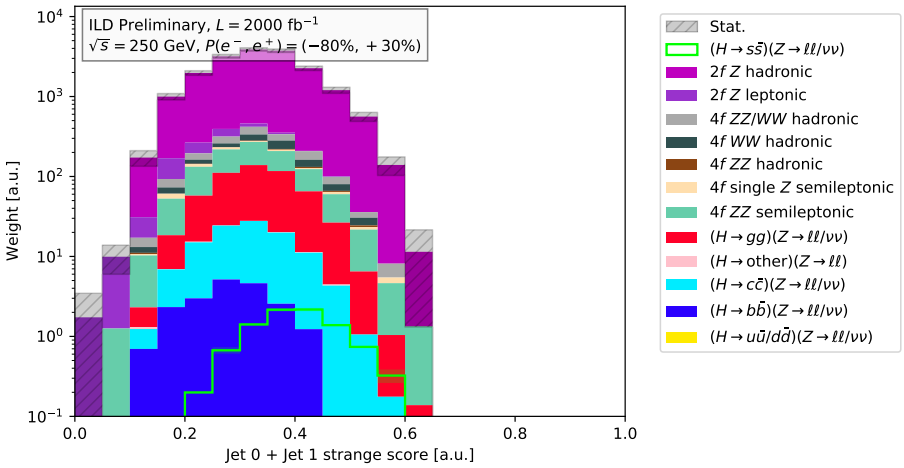

(a) $Z \to \nu\bar{\nu}$ channel

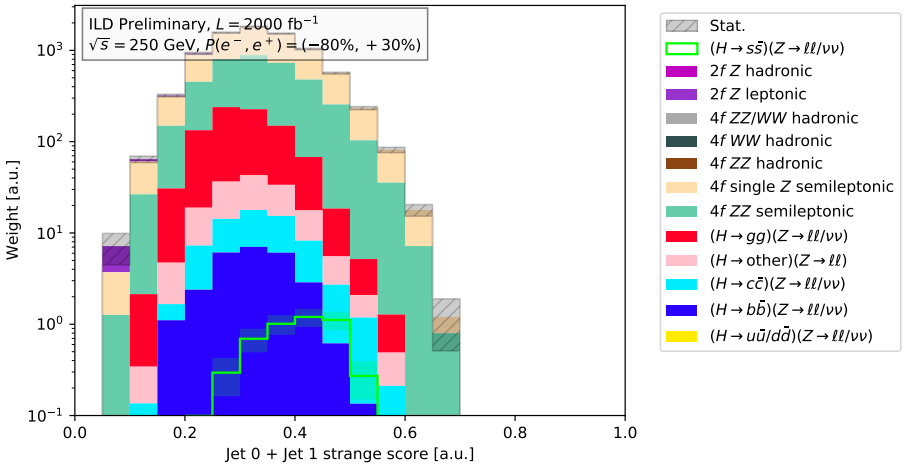

(b) $Z \to \ell\ell$ channel

Figure 12: Fit discriminant for the SM $h \to s\bar{s}$ analysis: ($0.5\times$) the sum of the strange scores for leading and subleading jets, using the jet flavour tagger described in Section 4. Each histogram is produced at the level of the last selection of their respective channel in Table 3. The error bars represent the Poisson counting uncertainties on those yields. The sum-of-weights per process is normalised to the SM cross-section. N.B. the $h(\to s\bar{s})Z(\to \ell\ell/\nu\bar{\nu})$ signal is unstacked.

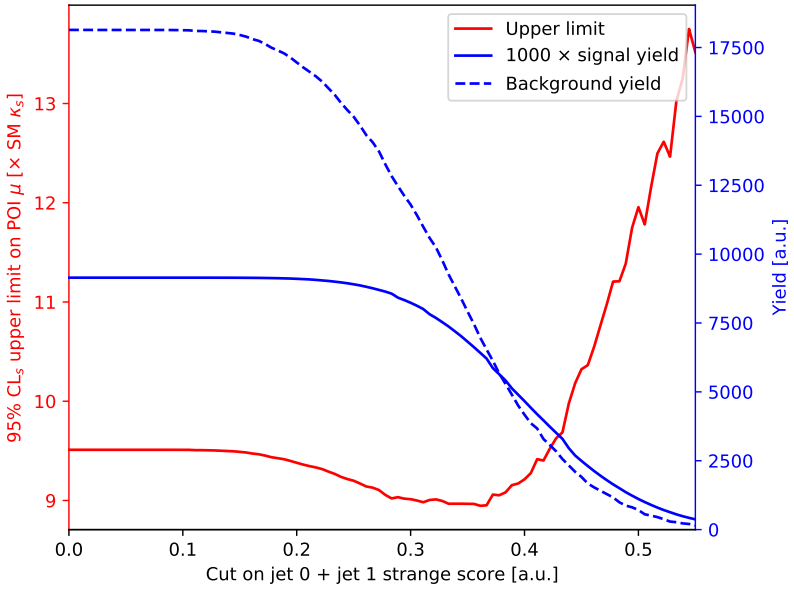

(a) $Z \to \nu\bar{\nu}$ channel

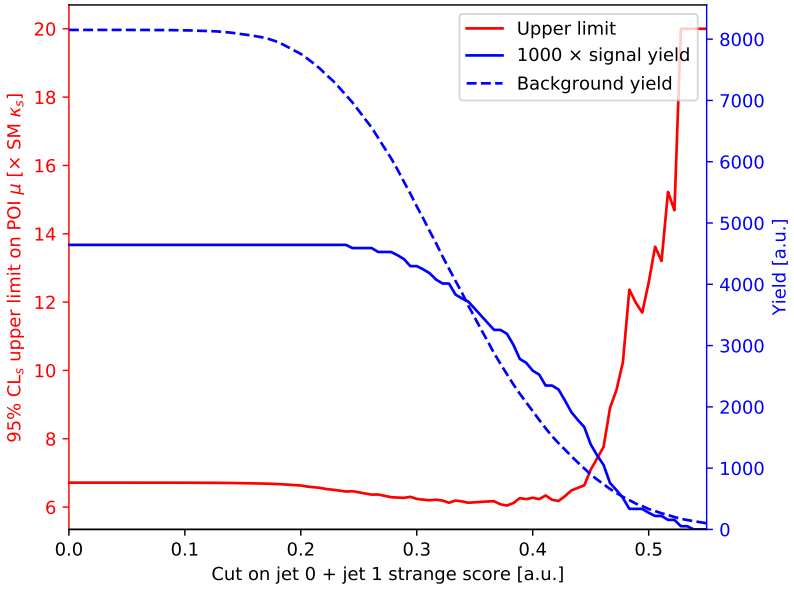

(b) $Z \to \ell\ell$ channel

Figure 13: Scans of the 95% CL_s upper limit for the Higgs-strange coupling strength modifier κ_s, obtained by varying the choice of the lower thresholds on the discriminants shown in Figure 12. Also shown are the signal (i.e., $h(\to s\bar{s})Z(\to \ell\ell/\nu\bar{\nu})$) and background (i.e., non-$h(\to s\bar{s})Z(\to \ell\ell/\nu\bar{\nu})$) yields in the resulting regions.

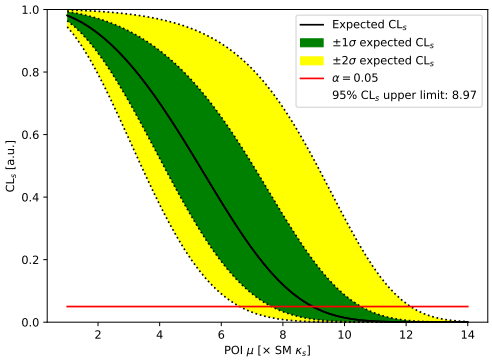

(a) $Z \to \nu\bar{\nu}$ channel

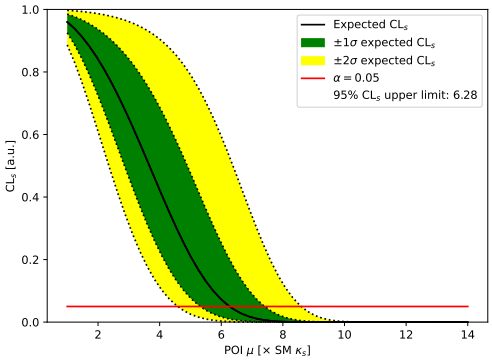

(b) $Z \to \ell\ell$ channel

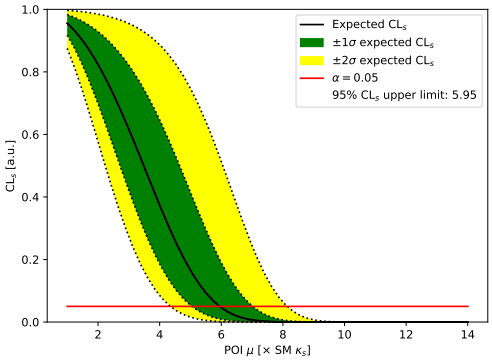

(c) Combined

Figure 14: CL_s upper limit plots for the Higgs-strange coupling strength modifier κ_s obtained from fitting the discriminants (in the regions >0.35 and >0.4 for the $Z \to \nu\bar{\nu}$ and $Z \to \ell\ell$ channels, respectively) shown in Figure 12. Only a single bin is used for each channel – the combination fit using both of these bins is also shown. The crossing of the black and red lines indicates the 95% confidence level.

6 Proposal for an alternative detector layout

[TODO: Add studies on RICH etc]

7 Conclusion

[TODO: Write a conclusion...]

References

[1] L. Evans and P. Bryant, J. Instrum. **3**, S08001 (2008). DOI 10.1088/1748-0221/3/08/S08001. URL https://www.doi.org/10.1088/1748-0221/3/08/S08001

[2] The ATLAS Collaboration, J. Instum. **3**, S08003 (2008). DOI 10.1088/1748-0221/3/08/S08003. URL https://www.doi.org/10.1088/1748-0221/3/08/S08003

[3] The CMS Collaboration, J. Instrum. **3**, S08004 (2008). DOI 10.1088/1748-0221/3/08/S08004. URL https://www.doi.org/10.1088/1748-0221/3/08/S08004

[4] The ATLAS Collaboration, Phys. Lett. B **812**, 135980 (2021). DOI 10.1016/j.physletb.2020.135980. URL https://www.doi.org/10.1016/j.physletb.2020.135980

[5] The CMS Collaboration, J. High Energ. Phys. **148** (2021). DOI 10.1007/JHEP01(2021)148. URL https://www.doi.org/10.1007/JHEP01(2021)148

[6] Y. Nakai, D. Shih, and S. Thomas, Strange Jet Tagging (2020). URL https://arxiv.org/abs/2003.09517

[7] J. Erdmann, J. Instrum. **15**(01), P01021 (2020). DOI 10.1088/1748-0221/15/01/P01021. URL https://www.doi.org/10.1088/1748-0221/15/01/P01021

[8] J. Duarte-Campderros, G. Perez, M. Schlaffer, and A. Soffer, Phys. Rev. D **101**(11), 115005 (2020). DOI 10.1103/PhysRevD.101.115005. URL https://www.doi.org/10.1103/PhysRevD.101.115005

[9] The CMS Collaboration, J. High Energ. Phys. **12**, 178 (2015). DOI 10.1007/JHEP12(2015)178. URL https://www.doi.org/10.1007/JHEP12(2015)178

[10] A. Djouadi and R. M. Godbole, *Electroweak symmetry breaking at the LHC* (2009), pp. 47–74. DOI 10.1007/978-81-8489-295-6_5. URL https://www.doi.org/10.1007/978-81-8489-295-6_5

[11] The ATLAS Collaboration, J. High Energ. Phys. **07**, 127 (2018). DOI 10.1007/JHEP07(2018)127. URL https://www.doi.org/10.1007/JHEP07(2018)127

[12] W. Altmannshofer, J. Eby, S. Gori, M. Lotito, M. Martone, and D. Tuckler, Phys. Rev. D **94**(11), 115032 (2016). DOI 10.1103/PhysRevD.94.115032. URL https://www.doi.org/10.1103/PhysRevD.94.115032

[13] W. Kilian, T. Ohl, and J. Reuter, Eur. Phys. J. C **71**, 1742 (2011). DOI 10.1140/epjc/s10052-011-1742-y. URL https://www.doi.org/10.1140/epjc/s10052-011-1742-y

[14] O. Wendt, F. Gaede, and T. Kramer, Pramana **69**, 1109 (2007). DOI 10.1007/s12043-007-0237-8. URL https://www.doi.org/10.1007/s12043-007-0237-8

[15] H. Aihara and others, SiD Letter of Intent. Tech. rep. (2009). URL https://arxiv.org/abs/0911.0006

[16] K. Fujii and others, ILC Study Questions for Snowmass 2021. Tech. rep. (2020). URL https://arxiv.org/abs/2007.03650

[17] Division of Particles and Fields. Particle Physics Community Planning Exercise (Snowmass). URL https://snowmass21.org

[18] T. Behnke, J. E. Brau, B. Foster, J. Fuster, M. Harrison, J. M. Paterson, M. Peskin, M. Stanitzki, N. Walker, and H. Yamamoto, The International Linear Collider Technical Design Report - Volume 1: Executive Summary. Tech. rep. (2013). URL https://arxiv.org/abs/1306.6327

[19] T. Abe and others, The International Large Detector: Letter of Intent. Tech. rep. (2010). DOI 10.2172/975166. URL https://www.doi.org/10.2172/975166

[20] T. Behnke, J. E. Brau, P. N. Burrows, J. Fuster, M. Peskin, M. Stanitzki, Y. Sugimoto, S. Yamada, and H. Yamamoto, The International Linear Collider Technical Design Report - Volume 4: Detectors. Tech. rep. (2013). URL https://arxiv.org/abs/1306.6329

[21] H. Abramowicz and others, The ILD detector at the ILC. Tech. rep. (2019). URL https://arxiv.org/abs/1912.04601

[22] M. A. Thomson, Nucl. Instrum. Meth. A **611**, 25 (2009). DOI 10.1016/j.nima.2009.09.009. URL https://www.doi.org/10.1016/j.nima.2009.09.009

[23] W. Kilian, T. Ohl, and J. Reuter. WHIZARD v2.8.5 (2020). URL https://gitlab.tp.nt.uni-siegen.de/whizard/public/-/releases#v2.8.5

[24] T. Sjostrand, S. Mrenna, and P. Z. Skands, J. High Energ. Phys. **05**, 026 (2006). DOI 10.1088/1126-6708/2006/05/026. URL https://www.doi.org/10.1088/1126-6708/2006/05/026

[25] S. Jadach, J. H. Kuhn, and Z. Was, Comput. Phys. Commun. **64**, 275 (1990). DOI 10.1016/0010-4655(91)90038-M. URL https://www.doi.org/10.1016/0010-4655(91)90038-M

[26] P. Golonka, B. Kersevan, T. Pierzchala, E. Richter-Was, Z. Was, and M. Worek, Comput. Phys. Commun. **174**, 818 (2006). DOI 10.1016/j.cpc.2005.12.018. URL https://www.doi.org/10.1016/j.cpc.2005.12.018

[27] N. Davidson, G. Nanava, T. Przedzinski, E. Richter-Was, and Z. Was, Comput. Phys. Commun. **183**, 821 (2012). DOI 10.1016/j.cpc.2011.12.009. URL https://www.doi.org/10.1016/j.cpc.2011.12.009

[28] D. Schulte, Beam-beam simulations with GUINEA-PIG. Tech. rep. (1999). URL http://cds.cern.ch/record/382453

[29] T. Ohl, Comput. Phys. Commun. **101**, 269 (1997). DOI 10.1016/S0010-4655(96)00167-1. URL https://www.doi.org/10.1016/S0010-4655(96)00167-1

[30] T. Ohl, CIRCE version 2.0: Beam spectra for simulating linear collider physics. Tech. rep. (2014). URL https://whizard.hepforge.org/circe2.pdf

[31] S. Agostinelli and others, Nucl. Instrum. Meth. A **506**, 250 (2003). DOI 10.1016/S0168-9002(03)01368-8. URL https://www.doi.org/10.1016/S0168-9002(03)01368-8

[32] P. Mora de Freitas, and H. Videau, in *International Workshop on Linear Colliders (LCWS 2002)* (2002), pp. 623–627

[33] F. Gaede, T. Behnke, N. Graf, and T. Johnson. iLCSoft/LCIO v02-15-04 (2020). URL https://github.com/iLCSoft/LCIO/releases/tag/v02-15-04

[34] F. Gaede, T. Behnke, N. Graf, and T. Johnson, in *International Conference on Computing in High Energy and Nuclear Physics (CHEP 2003)*, vol. C0303241 (2003), vol. C0303241, p. TUKT001. URL https://arxiv.org/abs/physics/0306114

[35] S. Kawada, in *International Workshop on Future Linear Colliders (LCWS 2021)* (2021). URL https://arxiv.org/abs/2105.08622

[36] T. Suehara and T. Tanabe, Nucl. Instrum. Meth. A **808**, 109 (2016). DOI 10.1016/j.nima.2015.11.054. URL https://www.doi.org/10.1016/j.nima.2015.11.054

[37] P. Chen, T. L. Barklow, and M. E. Peskin, Phys. Rev. D **49**, 3209 (1994). DOI 10.1103/PhysRevD.49.3209. URL https://www.doi.org/10.1103/PhysRevD.49.3209

[38] J. List, G. Moortgat-Pick, and J. Reuter, *Optimising the ILC Setup: Physics Programme, Running Scenarios and Design Choices* (2018). DOI 10.3204/PUBDB-2018-00782/B1. URL https://www.doi.org/10.3204/PUBDB-2018-00782/B1

[39] P. A. Zyla and others, Prog. Theor. Exp. Phys. **2020**(8), 083C01 (2020). DOI 10.1093/ptep/ptaa104. URL https://www.doi.org/10.1093/ptep/ptaa104

[40] Chollet, François and others. Keras (2015). URL https://keras.io

[41] M. Abadi and others. TensorFlow: Large-Scale Machine Learning on Heterogeneous Systems (2015). URL https://www.tensorflow.org

[42] J. Erdmann, O. Nackenhorst, and S. V. Zeißner, J. Instrum. **16**(08), P08039 (2021). DOI 10.1088/1748-0221/16/08/P08039. URL https://www.doi.org/10.1088/1748-0221/16/08/P08039

[43] K. Cho, B. van Merrienboer, Ç. Gülçehre, F. Bougares, H. Schwenk, and Y. Bengio, in *Proceedings of the 2014 Conference on Empirical Methods in Natural Language Processing (EMNLP)* (2014). URL http://arxiv.org/abs/1406.1078

[44] G. Klambauer, T. Unterthiner, A. Mayr, and S. Hochreiter, in *31st Conference on Neural Information Processing Systems (NIPS 2017)* (2017). URL http://arxiv.org/abs/1706.02515

[45] D.P. Kingma, J. Ba, in *3rd International Conference on Learning Representations, ICLR 2015, San Diego, CA, USA, May 7-9, 2015, Conference Track Proceedings* (2015). URL http://arxiv.org/abs/1412.6980

[46] The ATLAS Collaboration, Extrapolation of ATLAS sensitivity to $H \to b\bar{b}$ and $H \to c\bar{c}$ decays in VH production at the HL-LHC. Tech. rep. (2021). URL https://cds.cern.ch/record/2788490

[47] A. David, A. Denner, M. Duehrssen, M. Grazzini, C. Grojean, G. Passarino, M. Schumacher, M. Spira, G. Weiglein, and M. Zanetti, LHC HXSWG interim recommendations to explore the coupling structure of a Higgs-like particle. Tech. rep. (2012). URL https://arxiv.org/abs/1209.0040

[48] J. R. Andersen and others, Handbook of LHC Higgs Cross Sections: 3. Higgs Properties. Tech. rep. (2013). DOI 10.5170/CERN-2013-004. URL https://www.doi.org/10.5170/CERN-2013-004

[49] G. Cowan, K. Cranmer, E. Gross, and O. Vitells, Eur. Phys. J. C **71**, 1554 (2011). DOI 10.1140/epjc/s10052-011-1554-0. URL https://doi.org/10.1140/epjc/s10052-011-1554-0

[50] L. Heinrich, M. Feickert, and G. Stark. pyhf: v0.6.3. DOI 10.5281/zenodo.1169739. URL https://doi.org/10.5281/zenodo.1169739

[51] L. Heinrich, M. Feickert, G. Stark, and K. Cranmer, J. Open Source Softw. **6**(58), 2823 (2021). DOI 10.21105/joss.02823. URL https://doi.org/10.21105/joss.02823

[52] A. L. Read, J. Phys. G: Nucl. Part. Phys. **28**, 2693 (2002). DOI 10.1088/0954-3899/28/10/313. URL https://www.doi.org/10.1088/0954-3899/28/10/313

[53] J. de Blas and others, J. High Energ. Phys. **01**, 139 (2020). DOI 10.1007/JHEP01(2020)139. URL https://www.doi.org/10.1007/JHEP01(2020)139